X-525-66-84

NASA TM X-55506

COMPUTED RADIATION PATTERNS FOR A DUAL-PLANE AMPLITUDE-SENSING MONOPULSE ANTENNA USING AN ELECTRONIC BORESIGHT SCANNING TECHNIQUE

BY

ARMONDO D. ELIA
RICHARD F. SCHMIDT

GPO PRICE $ ______
CFSTI PRICE(S) $ ______

Hard copy (HC) 2.00
Microfiche (MF) .50

ff 653 July 65

FEBRUARY 1966

GODDARD SPACE FLIGHT CENTER
GREENBELT, MARYLAND

FACILITY FORM 602

N66 30329 (ACCESSION NUMBER)
(THRU)
33 (PAGES)
1 (CODE)
TMX-55506 (NASA CR OR TMX OR AD NUMBER)
02 (CATEGORY)

X-525-66-84

COMPUTED RADIATION PATTERNS FOR A DUAL-PLANE AMPLITUDE-SENSING MONOPULSE ANTENNA USING AN ELECTRONIC BORESIGHT SCANNING TECHNIQUE

by

Armondo D. Elia
and
Richard F. Schmidt

7 February 1966

Goddard Space Flight Center
Greenbelt, Maryland

COMPUTED RADIATION PATTERNS FOR A DUAL-PLANE AMPLITUDE-SENSING MONOPULSE ANTENNA USING AN ELECTRONIC BORESIGHT SCANNING TECHNIQUE

by

Armondo D. Elia
and
Richard F. Schmidt

ABSTRACT

30329

This report presents the scanned and unscanned radiation-pattern derived characteristics of an amplitude sensing monopulse antenna equipped with an Electronic Boresight Scanning circuit. A signal simulator, used for generating the monopulse antenna signals, is also presented.

Author

PRECEDING PAGE BLANK NOT FILMED.

CONTENTS

COMPUTED RADIATION PATTERNS FOR A DUAL-PLANE AMPLITUDE-SENSING MONOPULSE ANTENNA USING AN ELECTRONIC BORESIGHT SCANNING TECHNIQUE

INTRODUCTION

A method of analyzing an electronic boresight scanning (EBS) circuit (Figure 1) for a dual-plane amplitude-sensing monopulse system was presented by Elia and Schmidt [1]. The circuit was discussed in terms of the scattering-matrix formalism employed in the analysis of ferrite devices. A matrix product was developed in the referenced report to obtain a single transfer matrix relating the input-output quantities of the entire circuit composed of a conventional sum-and-difference network and the additional circuitry used to scan the monopulse patterns in space. In [1], a mathematical model of the circuit was utilized purely for convenience. The data presented in this report, however, is for a physically realizable model (See Figure 6b of [1]) and the phase shift domains of the scanning variable are changed accordingly. There is no significant difference between the mathematical and physical models discussed. The two versions are equivalent and the results presented in this report apply to both circuits.

An IBM computer was programmed to predict the operation of a 1705 Mc EBS system comprised of (1) A 15-foot parabolic reflector with F/D ratio of 0.400 (beam deviation factor 0.87), and monopulse feed with element displacement of $\sqrt{2}\,\lambda/4$ measured diagonally from boresight axis,(2) a standard sum-and-difference network (comparator), and (3) the scanning circuitry. Although the parameters of frequency and length, above, were made definite for computational

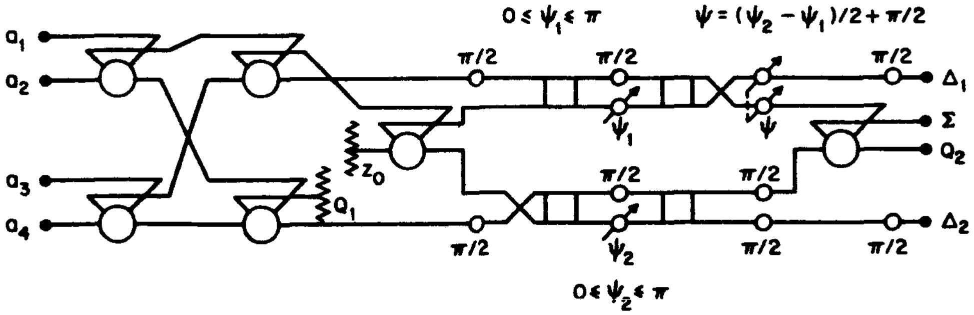

Figure 1–Electronic Boresight Scan Circuit

---

[1] Elia, A.D. and Schmidt, R.F., "A Chain Matrix Analysis of an Electronic Boresight Scanning Technique for a Dual-Plane Amplitude-Sensing Monopulse Antenna," Goddard Space Flight Center, Greenbelt, Md. Report X-525-65-300, 19 July 1965.

purposes, the program itself was entirely flexible so that parameters could be selected at will. The program utilized an idealized representation of the secondary-field patterns of the parabola and a transfer matrix representation of the radio-frequency circuitry. Linearly polarized components from separate orthogonal antennas were not explicitly introduced, therefore, the patterns can be regarded as circularly polarized throughout.

The region about boresight (the acquisition cone) was investigated by fixing the scanning variables (phase shifters) ψ_1 and ψ_2 in any given case, and selecting a cut or trajectory over the antenna in spherical coordinates $(1, \theta, \varphi)$. For every point on the trajectory, corresponding to the path of a satellite, the computer generated the received intensities of each of the four monopulse beams and then processed these signals according to the transfer matrix determined by the selected values of ψ_1 and ψ_2. The complex output quantities from the computer are: Σ (sum), Δ_1 (error), Δ_2 (error), Q_1 (quadrupolar load), and Q_2 (EBS load). These quantities (squared) can be compared to the energy received to verify the principle of energy conservation. Figure 2 shows the sequence of events in the computer.

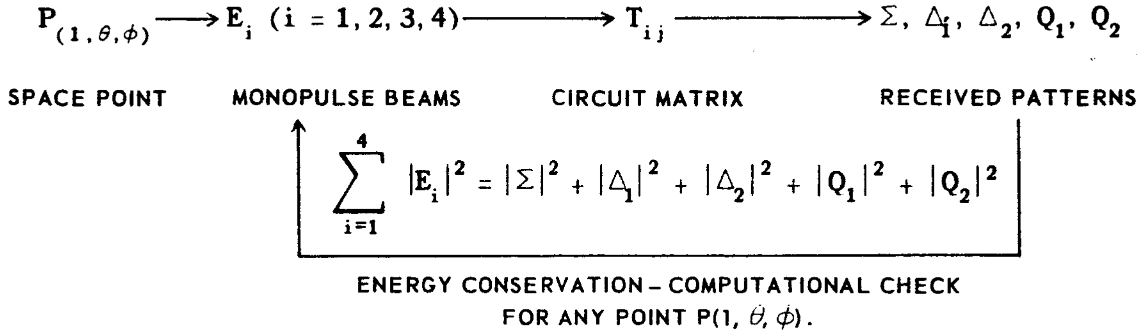

Figure 2–Simplified Flow Chart for EBS

The computer-generated monopulse antenna intensities were also simulated at 1705 Mc and applied to a coaxial version of the complete EBS circuit to determine the feasibility of the scanning technique. This represents an intermediate step between pure computation and evaluation by direct measurement on the antenna range. Details relating to the simulator and the pattern data obtained with the simulator are included in the Appendix of this report.

Radiation Patterns (The Unscanned System)

A representative set of patterns is presented in this report to illustrate the type of information which was made available through the analysis and computational effort on the EBS problem. Setting $\psi_1 = \psi_2 = 90°$, has the effect of making the entire circuit function as an ordinary sum-and-difference (comparator) network and there is no scanning of the monopulse patterns since the scanning variables are in the "rest" condition. $Q_2 \equiv 0$ for all θ, φ for this condition. Figure 3 illustrates the computed sum, difference, and load patterns for the principal-plane or θ-cut given by $\varphi = 0°$. The conventional sum pattern is observed, with a -3 db beamwidth of 3.2 degrees and should be compared to a -3 db beamwidth of 2.74 degrees for a single axial beam and cosine-taper illumination. In this principal plane $\Delta_2 = Q_1 = 0$ for all θ. The slope of Δ_1 is easily obtained by graphic means, and is discussed in detail in the section on scanned patterns.

Figure 4 depicts the four conventional monopulse outputs for another principal-plane or θ-cut given by $\varphi = 45°$. The figure is unique in that it belongs to one of two cuts for which the pattern Q_1 attains its maximum value. Ordinarily Q_1 is dissipated in a resistor for tracking operations and the information contained therein is not utilized. The other half of the cut, $\varphi = 225°$, is not shown here. It is noted, however, that unlike the error channels the phase of Q_1 is the same as in Figure 4 when φ 225° so that angle-tracking would not be associated with the Q_1 pattern. This figure is also unique in that the error-channel intensities are equal, $\Delta_1 = \Delta_2$ for all θ. A similar situation obtains when the orthogonal cut is given by $\varphi = 135°$ and $\varphi = 215°$.

Figure 5 represents a series of φ cuts of the sum channel for several constant values of θ. It is noted that the physical configuration of the antenna considered here exhibits perfect axial (rotational) symmetry as far as the reflector is concerned, but four-fold axial symmetry enters the configuration via the monopulse feed. The sum patterns taken about the Z-axis, Figure 5, illustrate four-fold symmetry for the ideal secondary patterns assumed in this investigation. For the parameters of frequency and length selected in the present computation, the effect is hardly noticeable at $\theta = 2°$, but becomes pronounced at $\theta = 4°$ as shown. It is also seen that a phase reversal has been suffered at $\theta = 6°$. In conclusion, the sum channel of a dual-plane monopulse antenna does not exhibit perfect axial symmetry even if the assumed secondary beams possess perfect rotational symmetry.

Figure 6 represents a series of φ cuts of one error channel (Δ_2) for several constant values of θ. The other error channel is identical to Δ_1, excepting that it is orthogonally disposed in space. In Figure 6, a measure of error channel slope is obtained by holding φ constant and noting the change of Δ_2 with θ; that is, slope $m = \partial\Delta_2/\partial\theta \,|_{\varphi=\text{const}}$. The error signal patterns illustrate $\Delta_2 = 0$ for all θ in the cut or trajectory given by $\varphi = 0°$ and $\varphi = 180°$. The region of highest sensitivity (error slope) corresponds to $\varphi = 90°$ and $\varphi = 180°$. A reduced error signal is observed beyond $\theta = 2°$, leading finally to a reversal of phase. As

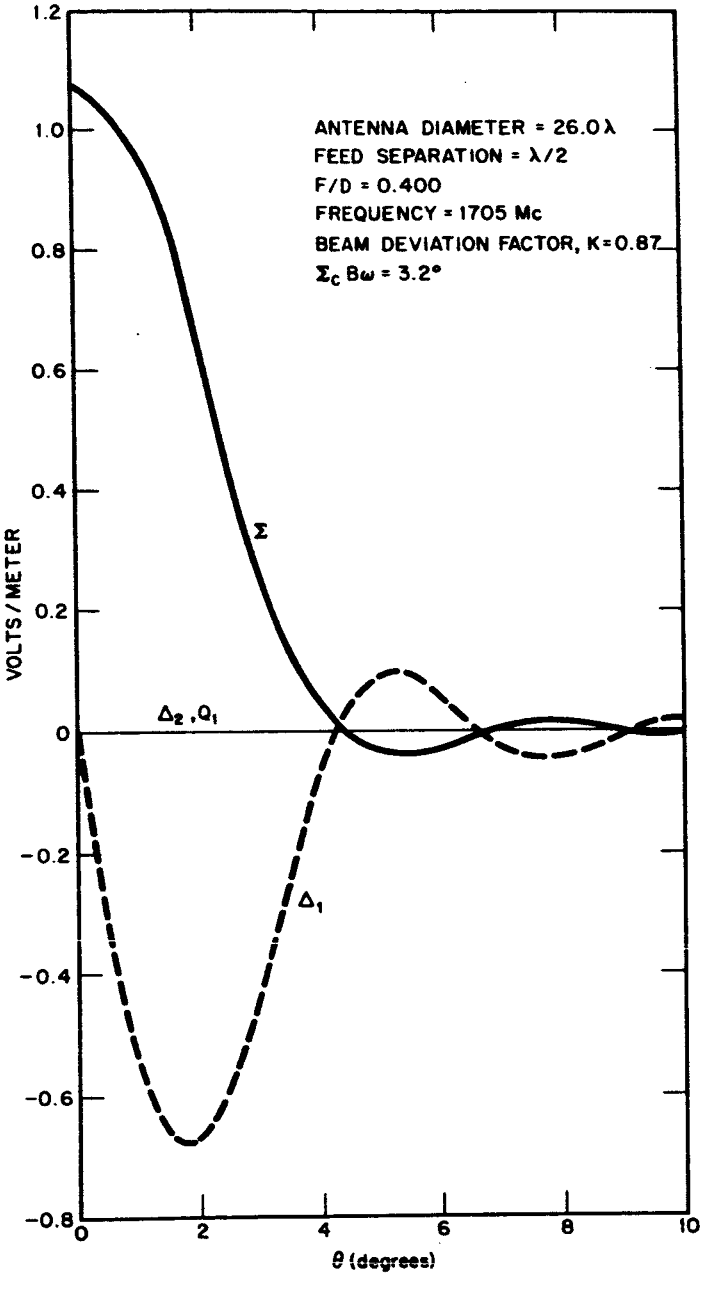

Figure 3—Radiation Patterns for an Unscanned Amplitude Sensing Monopulse Antenna ($\varphi = 0°$)

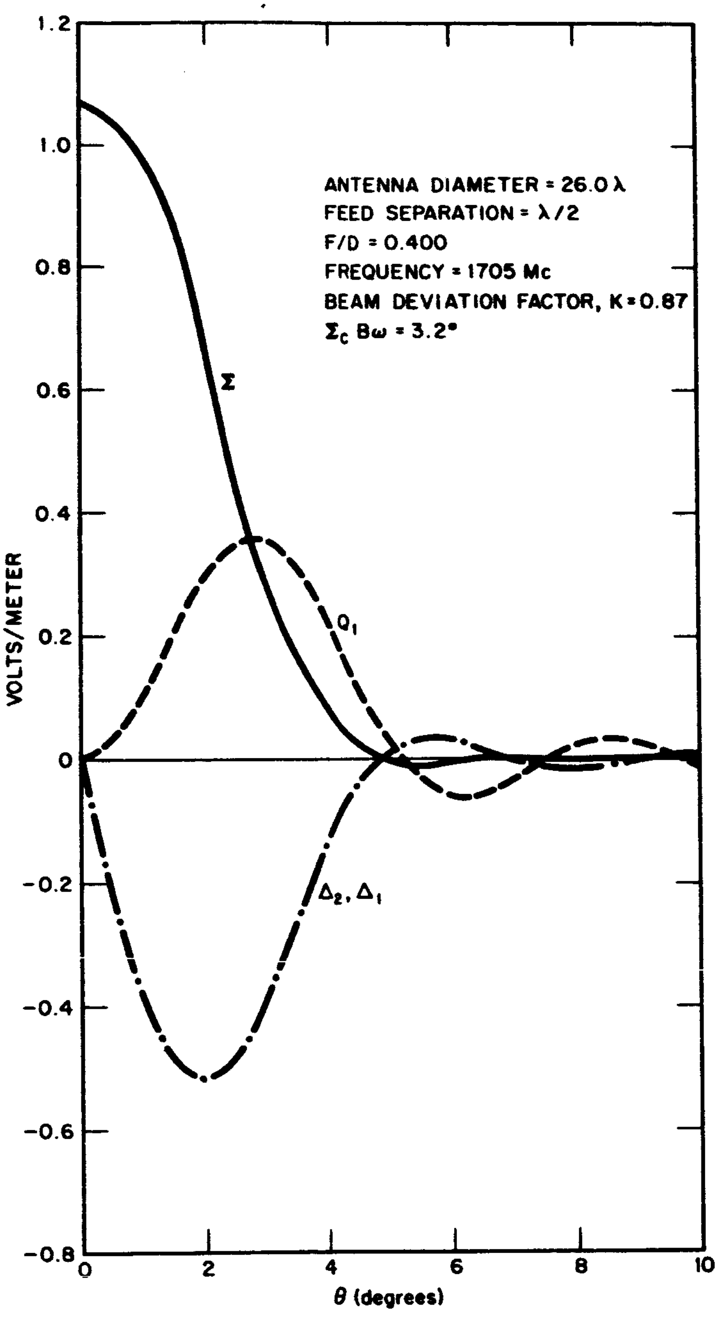

Figure 4–Radiation Patterns for an Unscanned Amplitude Sensing Monopulse Antenna ($\varphi = 45°$)

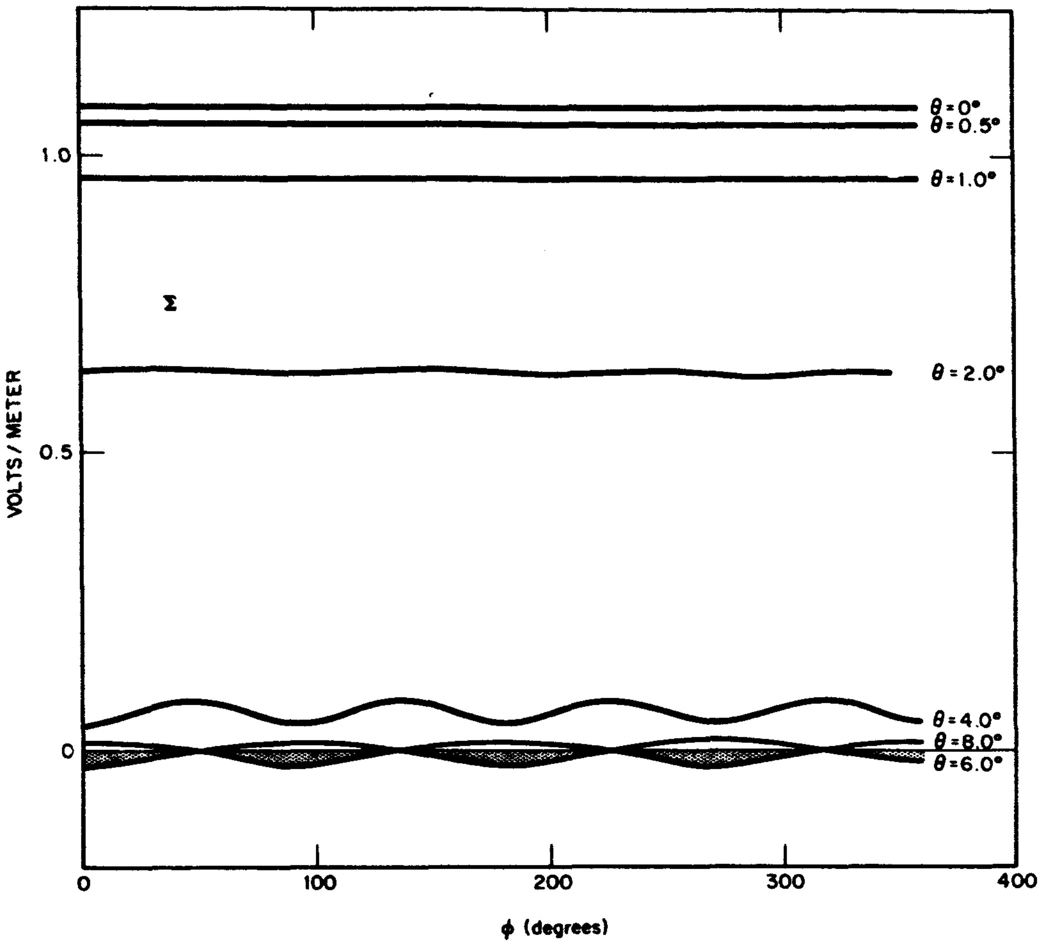

Figure 5–Sum Channel versus ϕ for constant θ

mentioned previously, the sum channel phase is reversed at $\theta = 6°$; therefore, the relative phase between Σ and Δ_2 at $\theta = 6°$ remains unchanged. The practical significance of tracking in this "fringe" region of the acquisition cone is certainly questionable; nevertheless, considerable insight is obtained about the nature of losing track or "lock".

Before proceeding with the problem of scanning the monopulse patterns in space, it may be helpful to consider the total energy in a conventional monopulse system. On the premise that the intercepts on four secondary squinted beams are known for any point $(1, \theta, \varphi)$ once the antenna parameters have been selected, it follows that the received energy has been implicitly stated. It is calculated as $\sum_1^4 |E_i|^2$ where the E_i are the four secondary beam intensities intersected by a plane wave. Figure 7 shows the variation of received (circuit) energy with angle

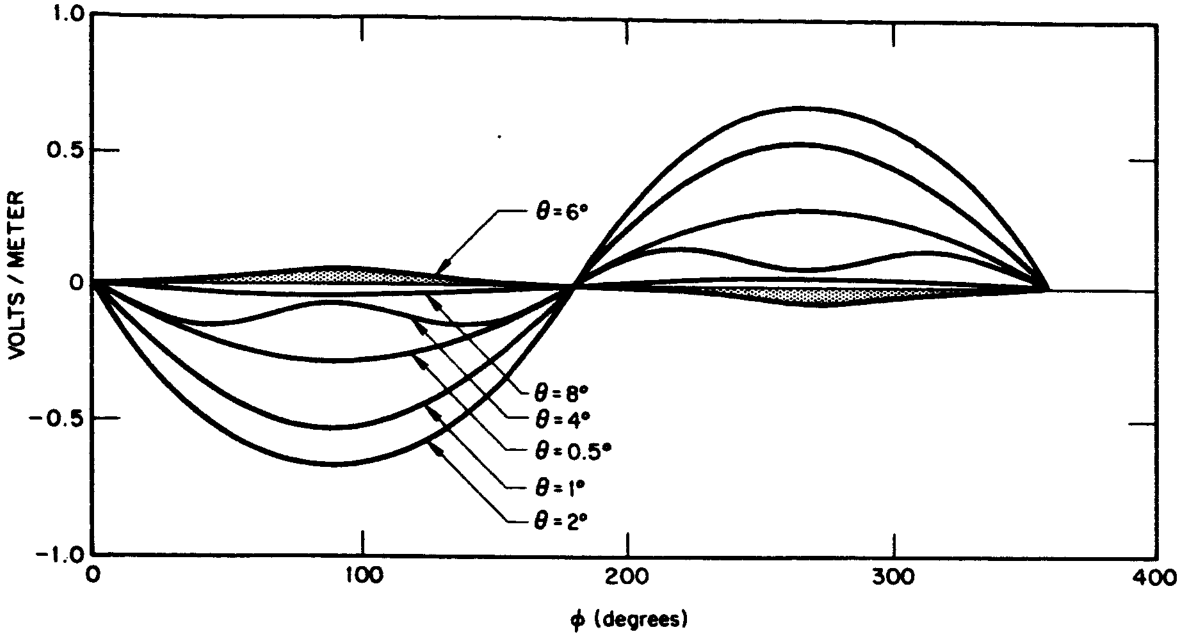

Figure 6–Error Channel (Δ_2) versus ϕ for Constant θ

θ for several values of φ. It can be seen that the circuit energy actually increases slightly for this antenna as θ increases from zero and then declines in a strictly monotonic fashion. Variation of antenna parameters can be expected to influence the curve of circuit energy versus θ, particularly the feed displacement from the focus (F), which determines the crossover levels among the secondary beams (E_i).

It may be worth noting that the energy contained in the error channels cannot be attributed to the reduction of signal in the sum channel. For example, if the energy in the various channels is given from the graphs of Figure 3, the following table can be constructed:

Table 1. Channel Energy vs. θ ($\varphi = 45°$)

θ (degrees)	$\lvert\Sigma\rvert^2$	$\lvert\Delta_1\rvert^2$	$\lvert\Delta_2\rvert^2$	$\lvert Q_1\rvert^2$	Total Energy
0	1.180	0	0	0	1.180
0.5°	1.100	.044	.044	.001	1.189
1.0°	.950	.144	.144	.020	1.258
1.5°	.760	.235	.235	.040	1.270
2.0°	.430	.250	.250	.080	1.014
2.8°	.130	.180	.180	.130	0.626
4.0°	.005	.013	.013	.036	0.067

These values are incongruous with the idea that error-channel energy is derived from an equal reduction of sum-channel energy.

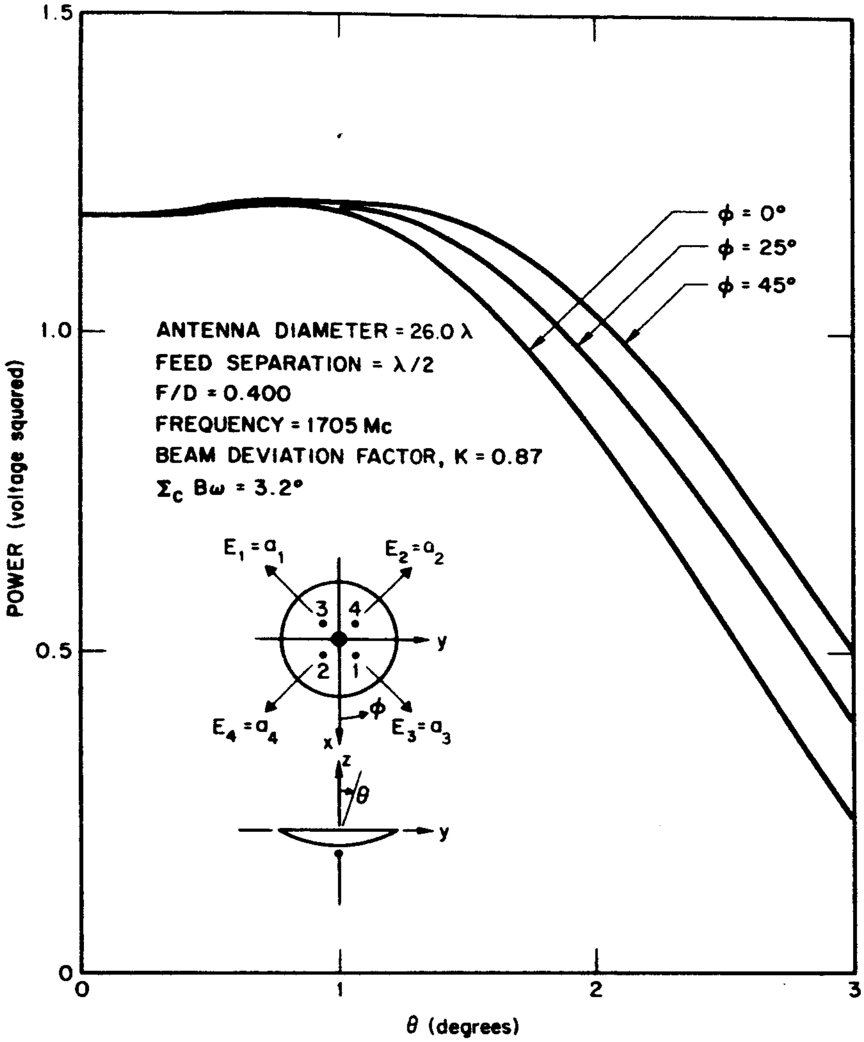

Figure 7–System Energy versus θ for Constant ϕ

Radiation Patterns (The Scanned System)

The EBS circuit considered here is intended for the displacement of monopulse patterns in two planes simultaneously. It is advantageous to examine the scanned system in a single plane, initially, by varying phase shifter ψ_2 while holding ψ_1 equal to 90°. Figure 8 shows the angular displacement (θ_n) of the simultaneous null ($\Delta_1 = \Delta_2 = 0$) versus ψ_2 for several feed-element separations (s). The same figure also shows the sum channel field intensity on the null bearing versus ψ_2, for the same feed-element separations. It is seen that the null-displacement is nearly linear with ψ_2, and that feed separation markedly affects the usefulness of the scanning technique considered here.

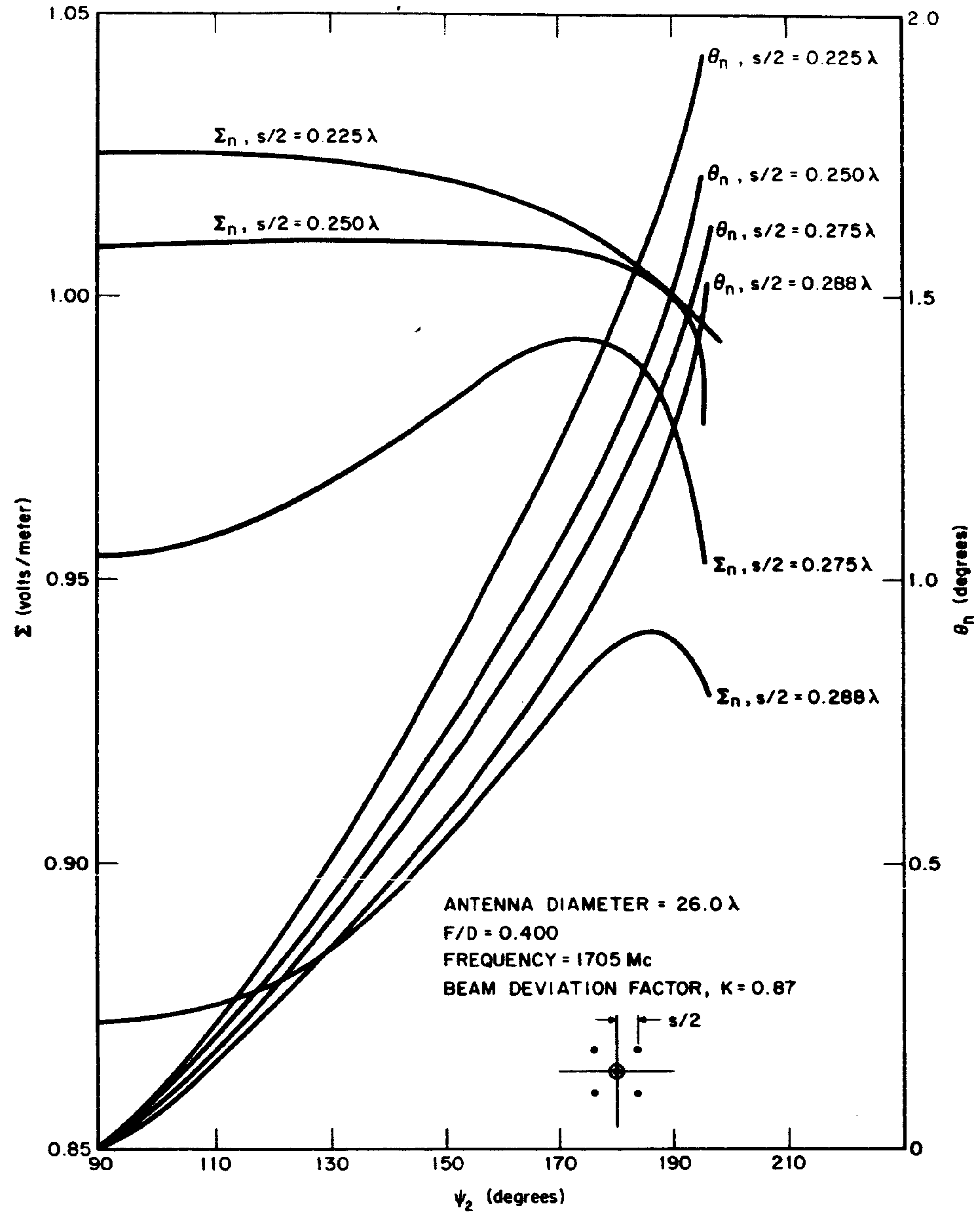

Figure 8—Sum Channel Intensity On Scanned Boresight And Boresight Position versus ψ_2 Degrees

A feed separation of $s/2 = 0.050\,\lambda$ (focal-plane element displacement of $\sqrt{2}\,\lambda/4$) appears to be about the best separation to achieve a nearly constant value of Σ_n along the bearing of the new simultaneous null over the latitude of scan. This figure also shows that the scanning capability of the present technique is about plus or minus one-half of the half-power beamwidth of the unscanned sum-channel beamwidth. For the 15-foot antenna investigated here at 1705 Mc, the -3 db beamwidth of Σ is 3.2° and the scanning capability about plus or minus 1.25° with approximately 180 degrees of phase shift (ψ_2 or ψ_1) required to achieve this result in a plane. The Σ_n intensity falls to -0.21 db below the unscanned Σ intensity at boresight for this example. If the null scanning is extended to plus or minus 1.60° in a plane, with approximately 102 degrees of phase shift, the Σ_n intensity falls to -0.38 db relative to the unscanned Σ intensity at boresight. The situation is similar when scanning in both planes.

It is noted that the amount of phase shift, ψ_1 or ψ_2, to scan the null over the sum beamwidth depends upon the relative magnitudes of the signals applied to each of the two scanning circuits. Dividing sum channel energy equally and applying $\Sigma/\sqrt{2}$ instead of Σ to the scanning circuits, or changing the feed spacing, for example, will generally affect the amount of phase shift required. A null is established at some position in space for an error channel when the quantity $|\Sigma \sin \psi_i/2 - \Delta_i \cos \psi_i/2|$ vanishes, where $i = 1, 2$ here. Then $\tan \psi_i/2 = \Delta_i/\Sigma$, $\Sigma \neq 0$. In the case where $\Sigma \rightarrow \Sigma/\sqrt{2}$, other factors being constant, the implication is that the domain of definition (ψ_i) is increased.

Figures 9, 10, 11, and 12 are field intensity plots versus θ, for two values of φ, and are therefore planar cuts. Scanning is by means of one variable (ψ_2) only for the first three figures and by means of both variables (ψ_2 and ψ_1), in equal amounts in the fourth figure. It can be seen that the Σ_n intensity is, in general, not the maximum value for a scanned Σ pattern. That is, the sum maximum and simultaneous null $\Delta_1 = \Delta_2 = 0$ have separated in space coordinates. It is also seen that that error channel slope will be reduced with increased scanning of the patterns and symmetry about boresight no longer exists. The maximum error channel amplitude is generally less than that of an unscanned system for $\theta = \theta_n$, where θ_n is the null bearing. The following table is constructed graphically using Figures 3, 9, 10 and 11:

Table II. Error Slope vs Phase Shift (ψ_2) $\varphi = 90°, 270°$

$\psi_2 = 90°$	$\|m\| \approx .8$ v/deg (unscanned)
$\psi_2 = 120°$	$\|m\| \approx .6$ v/deg (scanned)
$\psi_2 = 150°$	$\|m\| \approx .45$ v/deg (scanned)
$\psi_2 = 195°$	$\|m\| \approx .2$ v/deg (scanned)

Figures 4 and 12 provide the following information:

Table III. Error Slope vs Phase Shift (ψ_1 or ψ_2), $\varphi = 45°, 225°$

$\psi_1 = \psi_2 = 90°$	$\lvert m \rvert \approx .54$ v/deg. (unscanned)
$\psi_1 = \psi_2 = 150°$	$\lvert m \rvert \approx .23$ v/deg. (scanned)

Figure 12 also shows that the degradation of the Σ_n signal level for dual plane scanning is comparable to that obtained when scanning in a single plane.

Discussion of Results

This report has shown, by means of a representative number of radiation pattern cuts, that the analysis given in X-525-65-300 leads to meaningful results which are generally useful in the study and design of scanned and unscanned dual-plane, amplitude-sensing monopulse antennas. Upon selecting the antenna parameters and a suitable function for the secondary beams, the computer program is available for quantitative studies of the following: sum and error-channel intensities, error-channel slope, the relationship between null displacement and phase shift, symmetry effects, system energy and load-channel patterns.

The patterns presented in this report are restricted to planar cuts given by ($r = 1$, θ = variable, φ = constant) in the spherical coordinate frame. A more useful set of cuts can be obtained by determining the location of the scanned simultaneous null ($\Delta_1 = \Delta_2 = 0$) at $P_1 = (1, \theta_n, \varphi_n)$ and the scanned sum channel maximum at $P_2 = (1, \theta_m \varphi_m)$, and establishing a second spherical coordinate frame $(1, \theta', \varphi')$ so that the $x'y'$ plane of the latter contains points P_i and P_2. Planar cuts are then given about the displaced boresight as ($r' = 1$, θ' = variable, φ' = constant), where both θ and φ, of the first reference frame, now vary. This improvement has been carried out but was not available for presentation in this report.

In conclusion, a simulator is described in the Appendix of this report for generating monopulse antenna signals. The simulator is capable of generating signals for pure phase-sensing, pure amplitude-sensing, or phase-amplitude sensing antennas. By assumption, the mathematical representation for the parabolic antenna considered in this report was of the pure amplitude-sensing variety.

This report is part of a continuing analytical and experimental effort on the scanning of monopulse tracking patterns.

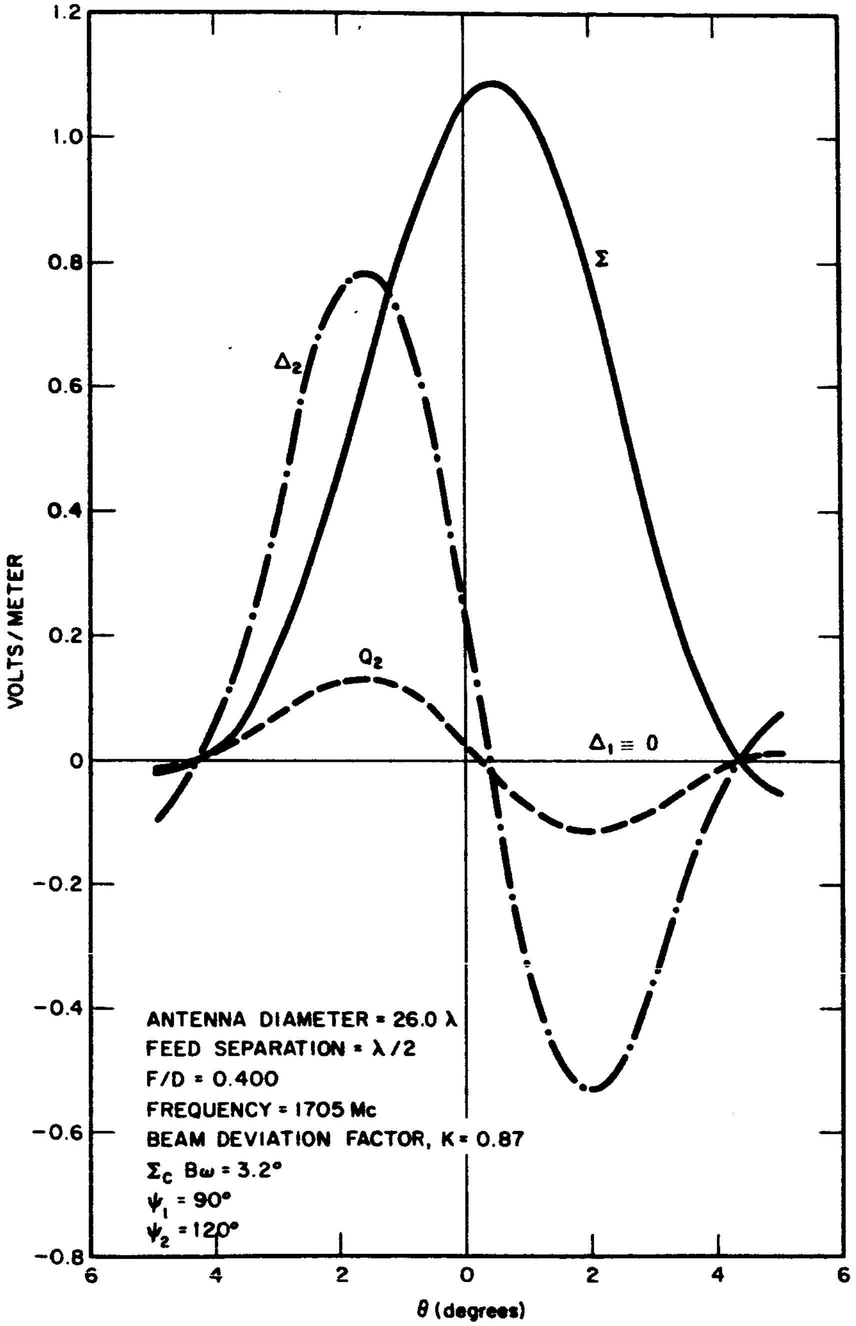

Figure 9–Radiation Patterns for a Scanned Amplitude Sensing Monopulse Antenna (φ = 90°, 270°)

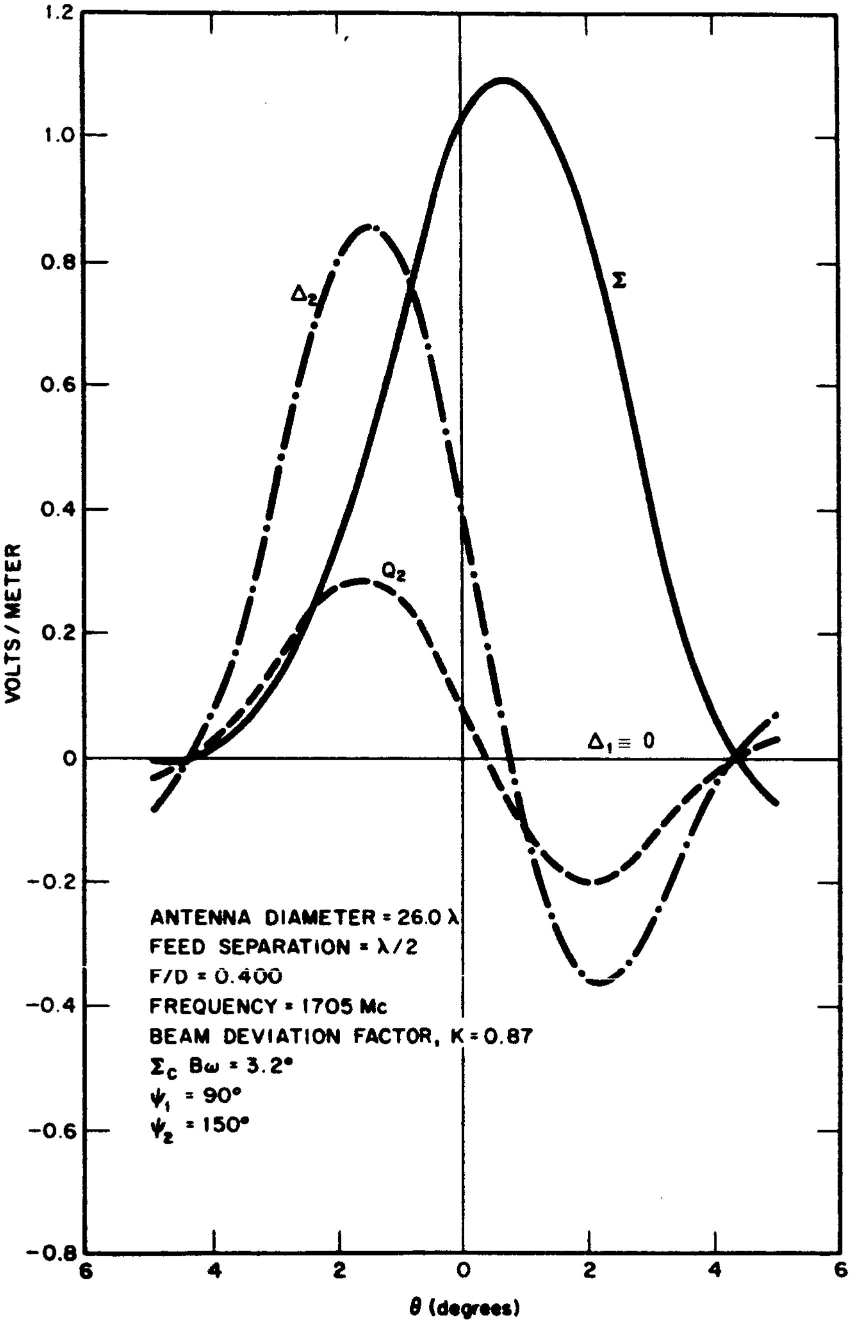

Figure 10–Radiation Patterns for a Scanned Amplitude Sensing Monopulse Antenna (ϕ = 90°, 270°)

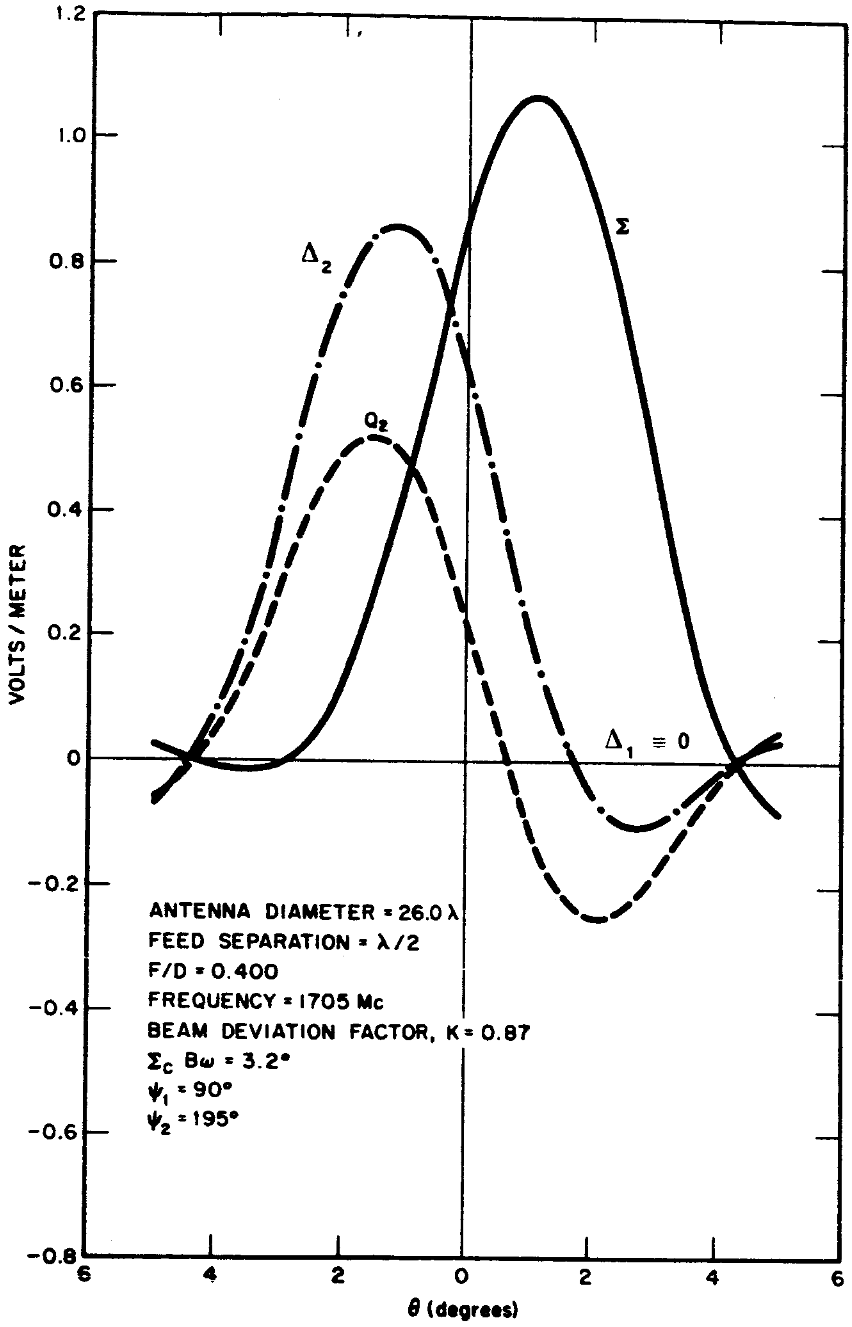

Figure 11—Radiation Patterns for a Scanned Amplitude Sensing Monopulse Antenna (ϕ = 90°, 270°)

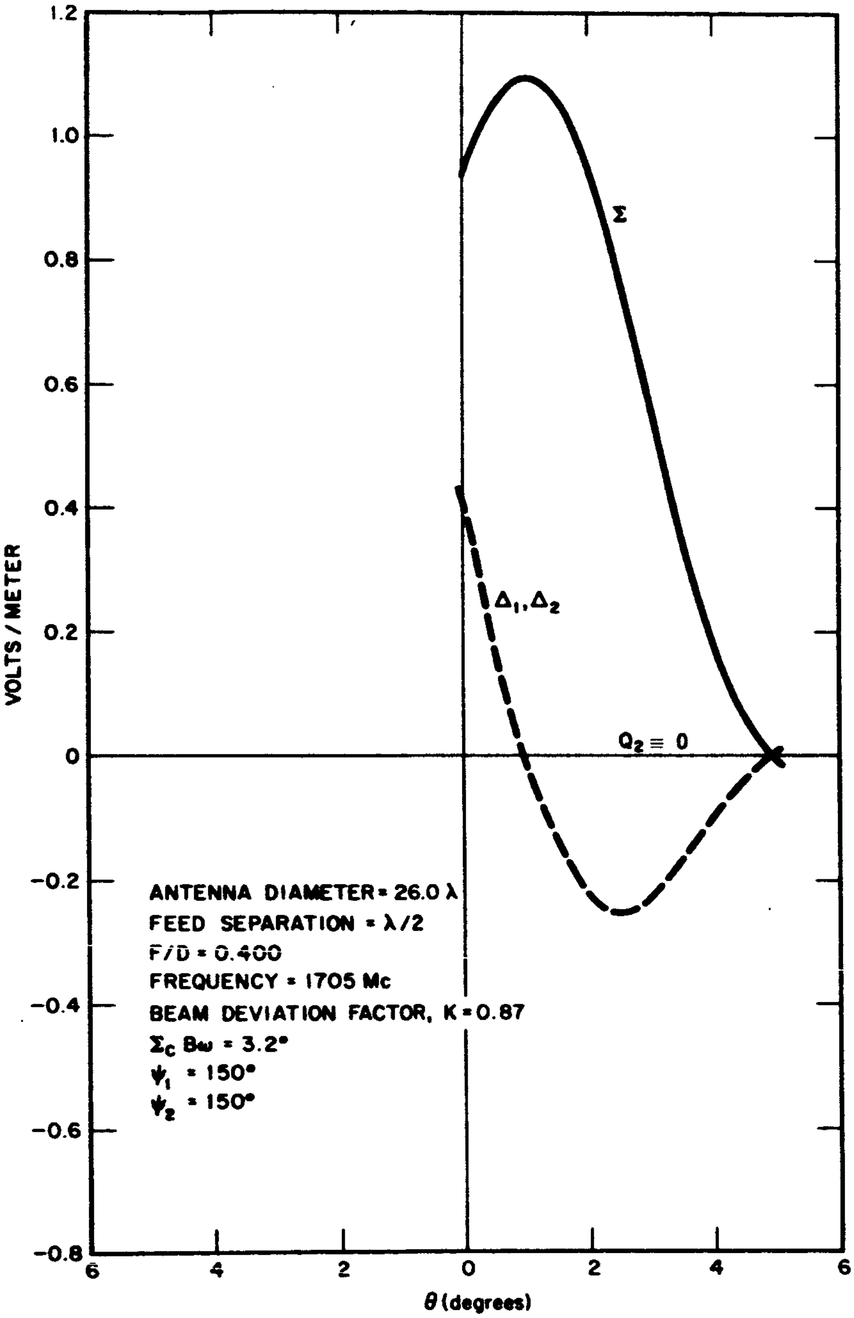

Figure 12–Radiation Patterns for a Scanned Amplitude Sensing Monopulse Antenna (ϕ = 45°, 225°)

APPENDIX I

Circuit Analysis

The mathematical formulation of a relationship between the inputs and outputs of the circuit shown in Figure 13 can be derived following the method developed in Reference 1. This method treats a circuit of this type in terms of the scattering-matrix analysis of ferrite devices. The end result is a matrix multiplication describing a transfer matrix (Teq) for the entire circuit giving the desired input-output relations. The scattering matrix and its associated transfer matrix for each type of junction used in Figure 1 is listed in Appendix IV of Reference 1.

In order to simplify the mathematical development, we shall only consider the case where one would obtain four output signals from one input signal; however, the reverse case where we would combine four signals to produce one signal as well as other variations of both cases may be handled within the framework of the existing mathematical development. Under the above simplification, the 8 × 8

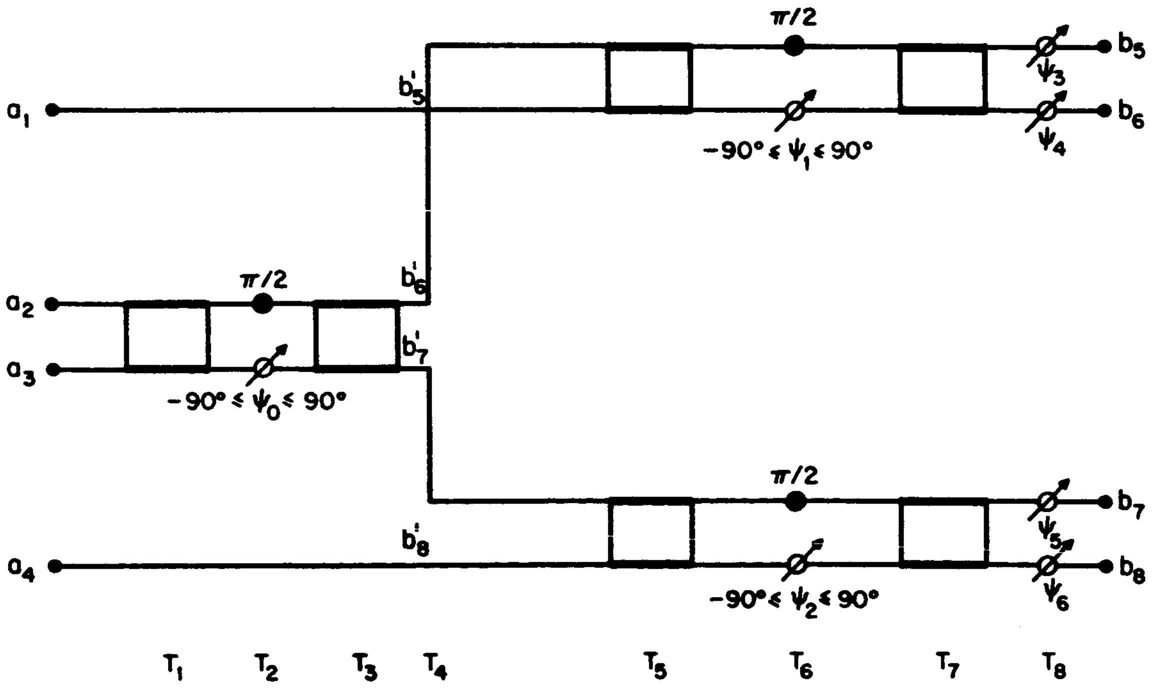

Figure 13–Signal Simulator

matrix that would result from the combined problem reduces to a 4×4 for the problem under consideration. This reduction is effected by deleting alternate rows from the square matrices and then deleting alternate columns from the resulting rectangular matrices.

The individual junctions utilized in this circuit can be described completely in terms of a scattering (S) matrix transformation. The scattering matrix transformation for each junction relates the output at a given port to the inputs at all ports and its elements are complex reflection and transmission coefficients in a physical circuit. The transfer (T) matrix transformation relates an output or an input on the "right" of a chain of junctions to the inputs and outputs on the "left" of that chain. Elements of the transfer matrix are complex transmission coefficients only. The respective transformations are given by $\bar{b} = S\,\bar{a}$ and $\bar{g} = T\bar{h}$.

Having listed the Tij matrix for each junction, we shall derive the Teq for the circuit as follows:

$$\mathrm{Teq} = T_8\, T_7\, T_6\, T_5\, T_4\, T_3\, T_2\, T_1$$

Using the assumptions stated above, i.e., only considering the circuit in one mode of operation and solving for Teq in several parts for convenience we have

$$\frac{1}{\sqrt{2}}\underset{T_7}{\left[\begin{array}{cc|cc} -j & -1 & 0 & 0 \\ -1 & -j & 0 & 0 \\ \hline 0 & 0 & -j & -1 \\ 0 & 0 & -1 & -j \end{array}\right]}\underset{T_6}{\left[\begin{array}{cc|cc} -j & 0 & 0 & 0 \\ 0 & e^{-j\psi_1} & 0 & 0 \\ \hline 0 & 0 & -j & 0 \\ 0 & 0 & 0 & e^{-j\psi_2} \end{array}\right]} = \frac{1}{\sqrt{2}}\underset{T_7\,T_6}{\left[\begin{array}{cc|cc} -1 & -e^{-j\psi_1} & 0 & 0 \\ j & -je^{-j\psi_1} & 0 & 0 \\ \hline 0 & 0 & -1 & -e^{-j\psi_2} \\ 0 & 0 & j & -je^{-j\psi_2} \end{array}\right]}$$

$$\frac{1}{\sqrt{2}}\underset{T_7\,T_6}{\begin{bmatrix} -1 & -e^{-j\psi_1} & 0 & 0 \\ j & -je^{-j\psi_1} & 0 & 0 \\ 0 & 0 & -1 & -e^{-j\psi_2} \\ 0 & 0 & j & -je^{-j\psi_2} \end{bmatrix}}\frac{1}{\sqrt{2}}\underset{T_5}{\begin{bmatrix} -j & -1 & 0 & 0 \\ -1 & -j & 0 & 0 \\ 0 & 0 & -j & -1 \\ 0 & 0 & -1 & -j \end{bmatrix}} = \frac{1}{2}\underset{T_7\,T_6\,T_5}{\begin{bmatrix} (j+e^{-j\psi_1}) & (1+e^{-j\psi_1}) & 0 & 0 \\ (1+je^{-j\psi_1}) & (-j-e^{-j\psi_1}) & 0 & 0 \\ 0 & 0 & (j+e^{-j\psi_2}) & (1+je^{-j\psi_2}) \\ 0 & 0 & (1+je^{-j\psi_2}) & (-j-e^{-j\psi_2}) \end{bmatrix}}$$

Similarly:

$$\underbrace{\begin{bmatrix} 1 & 0 & 0 & 0 \\ 0 & -j/\sqrt{2} & -1/\sqrt{2} & 0 \\ 0 & -1/\sqrt{2} & -j/\sqrt{2} & 0 \\ 0 & 0 & 0 & 1 \end{bmatrix}}_{T_3} \underbrace{\begin{bmatrix} 1 & 0 & 0 & 0 \\ 0 & -j & 0 & 0 \\ 0 & 0 & e^{-j\psi_0} & 0 \\ 0 & 0 & 0 & 1 \end{bmatrix}}_{T_2} = \underbrace{\begin{bmatrix} 1 & 0 & 0 & 0 \\ 0 & -1/\sqrt{2} & -e^{-j\psi_0}/\sqrt{2} & 0 \\ 0 & j/\sqrt{2} & -j e^{-j\psi_0}/\sqrt{2} & 0 \\ 0 & 0 & 0 & 1 \end{bmatrix}}_{T_3 T_2}$$

$$\underbrace{\begin{bmatrix} 1 & 0 & 0 & 0 \\ 0 & -1/\sqrt{2} & -e^{-j\psi_0}/\sqrt{2} & 0 \\ 0 & j/\sqrt{2} & -j e^{-j\psi_0}/\sqrt{2} & 0 \\ 0 & 0 & 0 & 1 \end{bmatrix}}_{T_3 T_2} \underbrace{\begin{bmatrix} 1 & 0 & 0 & 0 \\ 0 & -j/\sqrt{2} & -1/\sqrt{2} & 0 \\ 0 & -1/\sqrt{2} & -j/\sqrt{2} & 0 \\ 0 & 0 & 0 & 1 \end{bmatrix}}_{T_1} = \underbrace{\begin{bmatrix} 1 & 0 & 0 & 0 \\ 0 & \frac{1}{2}(j + e^{-j\psi_0}) & \frac{1}{2}(1 + j e^{-j\psi_0}) & 0 \\ 0 & \frac{1}{2}(1 + j e^{-j\psi_0}) & \frac{1}{2}(-j - e^{-j\psi_0}) & 0 \\ 0 & 0 & 0 & 1 \end{bmatrix}}_{T_3 T_2 T_1}$$

introducing the row permutation (T4) and the phase correction circuit (T8) we obtain

$$\underbrace{\begin{bmatrix} 0 & 1 & 0 & 0 \\ 1 & 0 & 0 & 0 \\ 0 & 0 & 1 & 0 \\ 0 & 0 & 0 & 1 \end{bmatrix}}_{T_4} \underbrace{\begin{bmatrix} 1 & 0 & 0 & 0 \\ 0 & \frac{1}{2}(j + e^{-j\psi_0}) & \frac{1}{2}(1 + j e^{-j\psi_0}) & 0 \\ 0 & \frac{1}{2}(1 + j e^{-j\psi_0}) & \frac{1}{2}(- j - e^{-j\psi_0}) & 0 \\ 0 & 0 & 0 & 1 \end{bmatrix}}_{T_3 T_2 T_1} =$$

$$\underset{T_4\,T_3\,T_2\,T_1}{\begin{bmatrix} 0 & \frac{1}{2}(j + e^{-j\psi_0}) & \frac{1}{2}(1 + je^{-j\psi_0}) & 0 \\ 1 & 0 & 0 & 0 \\ 0 & \frac{1}{2}(1 + je^{-j\psi_0}) & \frac{1}{2}(-j - e^{-j\psi_0}) & 0 \\ 0 & 0 & 0 & 1 \end{bmatrix}}$$

and

$$\underset{T_8}{\begin{bmatrix} e^{-j\psi_3} & 0 & 0 & 0 \\ 0 & e^{-j\psi_4} & 0 & 0 \\ 0 & 0 & e^{-j\psi_5} & 0 \\ 0 & 0 & 0 & e^{-j\psi_6} \end{bmatrix}} \underset{T_7\,T_6\,T_5}{\begin{bmatrix} (j + e^{-j\psi_1}) & (1 + je^{-j\psi_1}) & 0 & 0 \\ (1 + je^{-j\psi_1}) & (-j - e^{-j\psi_1}) & 0 & 0 \\ 0 & 0 & (j + e^{-j\psi_2}) & (1 + je^{-j\psi_2}) \\ 0 & 0 & (1 + je^{-j\psi_2}) & (-j - e^{-j\psi_2}) \end{bmatrix}} =$$

$$\underset{T_8\,T_7\,T_6\,T_5}{\frac{1}{2}\begin{bmatrix} e^{-j\psi_3}(j + e^{-j\psi_1}) & e^{-j\psi_3}(1 + je^{-j\psi_1}) & 0 & 0 \\ e^{-j\psi_4}(1 + je^{-j\psi_1}) & e^{-j\psi_4}(-j - e^{-j\psi_1}) & 0 & 0 \\ 0 & 0 & e^{-j\psi_5}(j + e^{-j\psi_2}) & e^{-j\psi_5}(1 + je^{-j\psi_2}) \\ 0 & 0 & e^{-j\psi_6}(1 + je^{-j\psi_2}) & e^{-j\psi_6}(-j - e^{-j\psi_2}) \end{bmatrix}}$$

Therefore

$$T_{eq} = \frac{1}{2}\begin{bmatrix} e^{-j\psi_3}(1 + je^{-j\psi_1}) & \frac{1}{2}(j + e^{-j\psi_0})e^{-j\psi_3}(j + e^{-j\psi_1}) & \frac{1}{2}(1 + je^{-j\psi_0})e^{-j\psi_3}(j + e^{-j\psi_1}) & 0 \\ e^{-j\psi_4}(-j - e^{-j\psi_1}) & \frac{1}{2}(j + e^{-j\psi_0})e^{-j\psi_4}(1 + je^{-j\psi_1}) & \frac{1}{2}(1 + je^{-j\psi_0})e^{-j\psi_4}(1 + je^{-j\psi_1}) & 0 \\ 0 & \frac{1}{2}(1 + je^{-j\psi_0})e^{-j\psi_5}(j + e^{-j\psi_2}) & \frac{1}{2}(-j - e^{-j\psi_0})e^{-j\psi_5}(j + e^{-j\psi_2}) & e^{-j\psi_5}(1 + je^{-j\psi_2}) \\ 0 & \frac{1}{2}(1 + je^{-j\psi_0})e^{-j\psi_6}(1 + je^{-j\psi_2}) & \frac{1}{2}(-j - e^{-j\psi_0})e^{-j\psi_6}(1 + je^{-j\psi_2}) & e^{-j\psi_6}(-j - e^{-j\psi_2}) \end{bmatrix}$$

using the equations

$$\bar{g} = T\bar{h}$$

we obtain the following input-output relationship for the case where $a_1 = a_3 = a_4 = 0$ for the simulator

$$b_5 = \frac{a_2}{4} (j + e^{-j\psi_0}) (j + e^{-j\psi_1}) e^{-j\psi_3} \tag{1}$$

$$b_6 = \frac{a_2}{4} (j + e^{-j\psi_0}) (1 + j e^{-j\psi_1}) e^{-j\psi_4} \tag{2}$$

$$b_7 = \frac{a_2}{4} (1 + j e^{-j\psi_0}) (j + e^{-j\psi_2}) e^{-j\psi_5} \tag{3}$$

$$b_8 = \frac{a_2}{4} (1 + j e^{-j\psi_0}) (1 + j e^{-j\psi_2}) e^{-j\psi_6} \tag{4}$$

Electrical Characteristics

One can deduce the electrical characteristics of the simulator by analyzing one section (say T3 T2 T1) and then applying the results to the entire circuit; therefore, performing the operation T3 T2 T1, we obtain

$$b_6' = \frac{a_2}{2} (j + e^{-j\psi_0})$$

$$b_7' = \frac{a_2}{2} (1 + j e^{-j\psi_0})$$

under the assumption that a_2 is the only input energized. Therefore, we obtain

$$b_6' = \frac{a_2}{2} \left[\cos \psi_0 + j\,(1 - \sin \psi_0)\right]$$

$$b_7' = \frac{a_2}{2} \left[(1 + \sin \psi_0) + j \cos \psi_0\right]$$

Expressing the above complex numbers in polar form we obtain

$$b_6' = \frac{a_2}{\sqrt{2}} \sqrt{1 - \sin \psi_0}\; e^{-j \tan^{-1}\left(\frac{1 - \sin \psi_0}{\cos \psi_0}\right)} \qquad (5)$$

$$b_7' = \frac{a_2}{\sqrt{2}} \sqrt{1 + \sin \psi_0}\; e^{-j \tan^{-1}\left(\frac{\cos \psi_0}{1 + \sin \psi_0}\right)} \qquad (6)$$

Considering just the amplitude part of the problem, a curve can be plotted, using the magnitude portion of equations 5 and 6, relating the ratio $R_0 = |b_6'| / |b_7'|$ to the amount of phase shift (φ_0) in degrees required to produce R_0. This relationship is shown graphically in Figure 14. Therefore, returning to the initial problem of producing four specific output signals from one input signal, one proceeds by letting

$$R_1 = \frac{|b_5|}{|b_6|}$$

and

$$R_2 = \frac{|b_7|}{|b_8|}$$

and then determining from Figure 2 the phase shifts required to produce R 1 and R2. To obtain the proper signal levels between the two weighting circuits contained in T7 T6 T5 , one would calculate R_0 from the relationship

$$R_0 = \frac{|b_6'|}{|b_7'|}$$

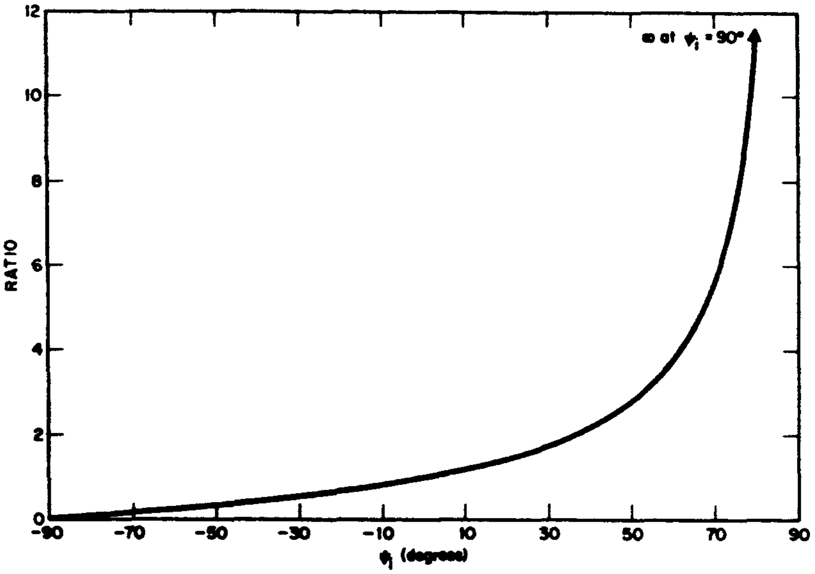

Figure 14–Ratio (R_i) Versus Phase Shift (ψ_i)

where

$$|b_6'| = \sqrt{|b_5|^2 + |b_6|^2}$$

and

$$|b_7'| = \sqrt{|b_7|^2 + |b_8|^2}$$

Therefore

$$R_0 = \frac{\sqrt{|b_5|^2 + |b_6|^2}}{\sqrt{|b_7|^2 + |b_8|^2}}$$

The weighting operation described for T3 T2 T1 will change the phase of the two output signals with respect to the input signal, and can cause the phase of the two output signals to change by 180° with respect to one another. This latter phase reversal can be avoided by a proper choice of the domain of phase shift for ψ_0 and the two output signals will remain co-phased. However, the change of phase of the output signals with respect to the input signals cannot be avoided, and this situation must be corrected when more than one weighting circuit is being employed if co-phased output signals are desired. Therefore, considering the entire circuit shown in Figure 1, a proper choice for ψ_0 will insure that b_6' and b_7' will remain co-phased for all R_0. The same can be said for ψ_1 in relation to b5 and b6, and ψ_2 for b7 and b8. However, if co-phased outputs are required, one must phase correct between the weighting circuits contained in T7 T6 T5 when $R1 \neq R2$. Each weighting circuit of T7 T6 T5 advances a signal, with respect to the input, by an amount $5\pi/4 - \psi_i/2$. In order to restore the initial phase relationship, we must delay a signal by this amount. This can be done by introducing two phase shifters at the output of each weighting circuit or the entire phase correction operation can be accomplished by phase-shifters ψ_3 and ψ_4. Since each circuit advances a signal by an amount $5\pi/4 - \psi_i/2$, we can derive a law such that

$$\psi_3 = \psi_4 = \frac{\psi_2 - \psi_1}{2}$$

will phase correct all four outputs. If any other phase condition is required, one may now introduce this into ψ_3, ψ_4, and ψ_5.

Simulated Patterns

The signal simulator was used to bench test a coaxial version of the EBS circuit as mentioned in the main part of this report. The output quantities of the four feed elements in the 15' parabolic antenna were readily available via a computer program; therefore, the electric field intensities corresponding to principal plane cuts (trajectories) over the antenna were simulated and then were used as inputs to a comparator circuit. The output quantities $\Sigma/\sqrt{2}$, $\Sigma/\sqrt{2}$, Δ_1, Δ_2 of the comparator were then used in the EBS circuit for scanning the boresight indication ($\Delta_1 = \Delta_2 = 0$). Figure 15 depicts one such operation where the experimental data, using the simulator, is superimposed upon the theoretical data for the scanning condition $\psi_1 = 90°$, $\psi_2 = 150°$.

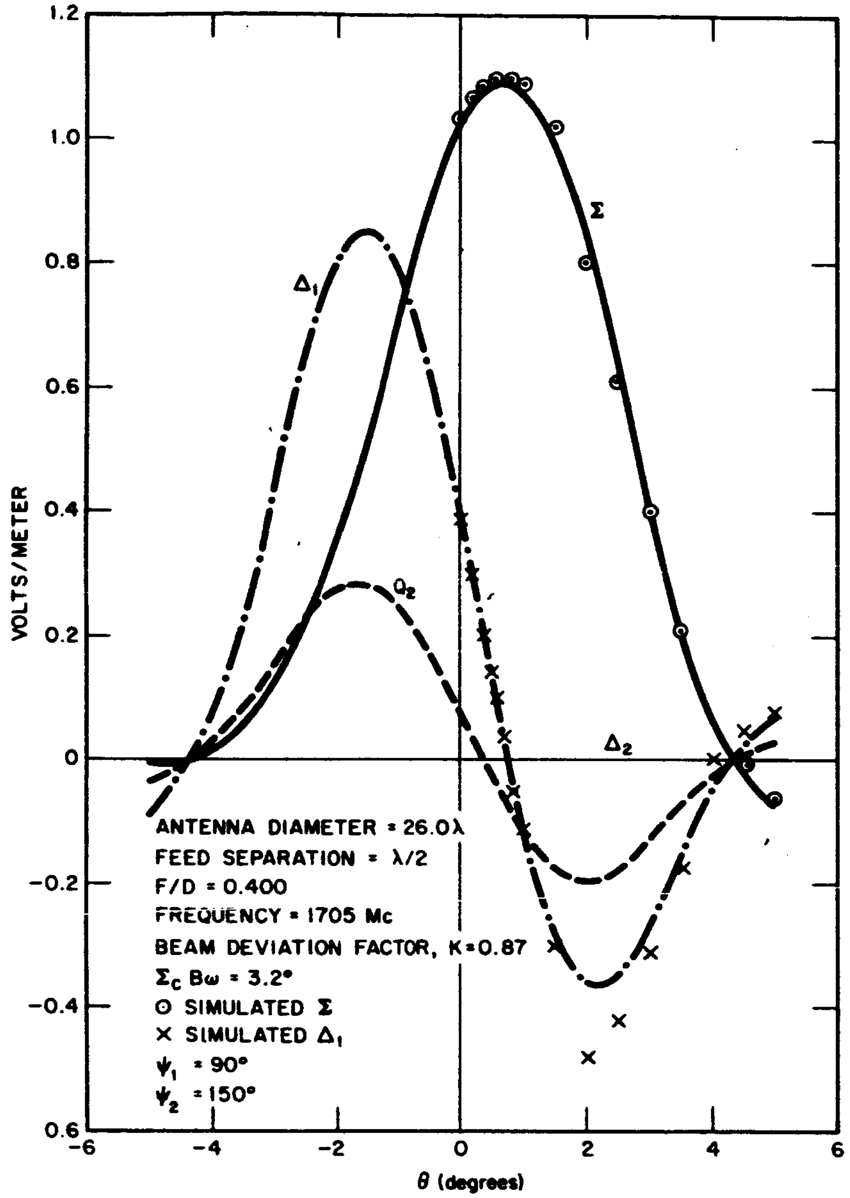

Figure 15–Experimental Data Superimposed upon Theoretical Data

ACKNOWLEDGMENTS

The assistance of the following Goddard Space Flight Center personnel is gratefully acknowledged. From the Antenna Systems Branch: Mr. George Winston for his comments pertaining to the servo-control problem, Mr. Kenneth Hanlin for a complete review of the matrix formulation and trigonometric reductions, Mr. William Welch for transfer matrix and aperture calculations, and Mr. Thomas Tunney for measurement of junction characteristics. From the Advanced Orbital Branch: Mr. William Carpenter and Mr. Phillip Merwarth for supporting computer calculations on the IBM 7094.